



Contents lists available at ScienceDirect



Catalysis Today

journal homepage: www.elsevier.com/locate/cattod

Synthesis of NiMo catalysts supported on mesoporous silica FDU-12 with different morphologies and their catalytic performance of DBT HDS

Xilong Wang^a, Peng Du^{a,1}, Kebin Chi^b, Aijun Duan^{a,*}, Chunming Xu^{a,*}, Zhen Zhao^a, Zhentao Chen^a, Honglei Zhang^a

^a State Key Laboratory of Heavy Oil Processing, China University of Petroleum, Beijing 102249, PR China

^b Petrochemical Research Institute, PetroChina Company Limited, Beijing 102206, PR China

ARTICLE INFO

Article history:

Received 31 July 2016

Received in revised form

26 September 2016

Accepted 25 October 2016

Available online xxx

Keywords:

FDU-12

Inorganic salts

Morphology

HDS

ABSTRACT

Mesoporous silica FDU-12 with remarkable morphologies such as hexagonal prisms, spiral rodlike and brick-like, were successfully synthesized under low temperature and strong acidic conditions by introducing of different inorganic salts. The products were characterized by Small-angle X-ray scattering (SAXS) patterns, UV-vis diffuse reflectance Spectroscopy, N₂ adsorption-desorption, scanning electron microscopy (SEM), laser Raman spectra (Raman), Fourier transform infrared spectroscopy with pyridine adsorption (pyridine-FTIR), X-ray photoelectron spectrometer (XPS), and transmission electron microscopy (TEM). The results showed that all the samples had high degrees of crystallinity, regular shape, large pore size and specific surface area, while the addition of different inorganic salts had a great influence on the morphology of FDU-12. Furthermore, the DBT HDS performances of FDU-12 supported NiMo hydrodesulfurization (HDS) catalysts were also investigated. The hexagonal prism NiMo/F-HP catalyst had a higher sulfurization degree and more acid sites than other catalysts. The catalytic results indicated that the morphologies and acidities of FDU-12 materials played an essential role in the catalytic performance of DBT HDS over NiMo catalysts. Among the catalysts with different morphologies, the DBT HDS conversions followed the order: hexagonal prism catalyst (NiMo/F-HP)>spiral catalyst (NiMo/F-SP)>brick-like catalyst (NiMo/F-BL). The highest activity of NiMo/F-HP could be ascribed to the relatively higher acidity, higher sulfurization degree and the better dispersion of the active phases.

© 2016 Elsevier B.V. All rights reserved.

1. Introduction

The environmental regulations impel the fuel specifications to reduce the sulfur amount in diesel fractions to near zero, then the relative researches are receiving much interest [1–3]. Hydrodesulfurization (HDS) of these fuel fractions is currently one of the major catalytic processes used in the petroleum refining industry. Most of the studies focus on the removal of the highly refractory molecules such as dibenzothiophene (DBT) and 4,6-dimethylbenzothiophene (4,6-DMDBT) [4–6]. In order to meet the stringent standards, the design and development of HDS catalysts with high activity and selectivity have been paid more

attention. Therefore, as the elementary compositions of the catalysts, the support materials play important role to realize the ultra deep removal of sulfur [7,8].

Since the discovery of M41S series mesoporous materials was published [9], the synthesis of different hierarchically porous materials becomes hotspots. Their outstanding texture parameters, such as highly ordered pore structures, adjustable pore size, large surface areas and huge pore volume, make them to be the available materials in the processes of adsorption [10], catalysis, separation, biomedicine [11], etc. In addition to the physical properties, the morphology of these materials, however, has a great influence on their applications in different areas. Till now, a few reports have described the methods to control the morphology of the mesoporous particles. Mesoporous SBA-15 silicas with four kinds of morphologies, including fiberlike, rodlike, platelet, were synthesized and used to evaluate the dynamic adsorption/desorption behavior of VOCs (C₇H₈) in a fixed bed unit [12]. The results showed that the interconnected rodlike SBA-15 silica exhibited extraordi-

* Corresponding authors.

E-mail addresses: duanaijun@cup.edu.cn, duanaijun@163.com (A. Duan), xcm@cup.edu.cn (C. Xu).

¹ This author has equal contribution as the first author.

nary good performance, a higher adsorption capacity, and better desorption performance for toluene. Gao et al. [13] reported the synthesis of mesoporous SBA-15 silicas with different morphologies. Using SBA-15 with sphere morphology as the support, the Al-SBA-15 supported NiMo hydrodesulfurization (HDS) catalyst exhibited the highest activities than the others (hexagonal prisms and rods morphologies). They ascribed the influence to the superior diffusion of the supports with sphere morphology and its better dispersion of the active components. Liu et al. [14] synthesized mesoporous silicas with various morphologies by modulating the weight ratios of 2,2,4-trimethylpentane (TMP)/P123. The results showed that mesoporous silica materials with hollow spheres morphology could greatly accelerate the adsorption rate of the enzyme during the adsorption process. Johansson et al. [15] found that particle morphology of mesoporous silica SBA-15 could be tuned by varying the HCl concentration.

FDU-12 mesoporous silicas with highly ordered face-centred cubic ($Fm\bar{3}m$) structure were firstly synthesized by Zhao and coworkers [16] using F127 as a template under strong acidic conditions. Due to their large surface areas and uniformly adjustable pore size, the materials have received much attention in the fields of adsorption, catalysis and pharmaceutical. Besides, the morphology of FDU-12 also has great influence on the activity of catalytic reactions [17,18].

Zhao et al. [19] reported that the macroscopic morphology of the mesoporous FDU-12 materials largely depended on the local curvature energy, which was manifested in the interface of the amphiphilic block copolymer species and inorganic silica. The local curvature energy could be tuned by adding different strong inorganic salts, which facilitated the formation of various morphologies. FDU-12 mesoporous materials with the morphologies of doughnut-like, hard/hollow sphere and hexagonal disk crystals have been reported [20]. It was found that divalent sulfates like $CuSO_4$, $NiSO_4$, $ZnSO_4$ or $MgSO_4$ were indispensable for the formation of ordered $Fm\bar{3}m$ pore structure, while K_2SO_4 and Na_2SO_4 is beneficial to generate hollow nanospheres.

In this research, a series of mesoporous silicas FDU-12 with remarkable morphologies were successfully synthesized by introducing different inorganic salts under acidic condition. The corresponding NiMo catalysts supported on the above mesoporous materials were prepared by two-step incipient-wetness impregnation method. The FDU-12 supports with different morphologies and the corresponding catalysts were characterized by SAXS, BET, SEM, TEM, UV-vis, Raman, pyridine-FTIR and XPS techniques. Furthermore, the effect of morphology on the HDS activity was investigated at different WHSVs using DBT as probe molecules. The DBT HDS activity followed the order: hexagonal prism catalyst (NiMo/F-HP) > spiral catalyst (NiMo/F-SP) > brick-like catalyst (NiMo/F-BL).

2. Experimental

2.1. Preparation of supports and catalysts

The synthesis procedure follows: 2.0 g of triblock copolymers F127, a certain amount of inorganic salt ($KCl/MgSO_4/MnCl_2$), 2.0 of 1,3,5-trimethylbenzene (TMB, Sinopharm Chemical Reagent, 98.0 wt%) were dissolved in 120 mL of 2.0 M HCl aqueous solution with vigorous stirring for 24 h. Then 8.3 g of tetraethyl orthosilicate (TEOS, Sinopharm Chemical Reagent, 99.0 wt%) as the silicate source was added dropwise into the above surfactant solution for another 24 h. Afterwards the mixture was transferred into a Teflon bottle and heated statically at 100 °C for 72 h. The final as-synthesized product was obtained by filtering, washing with distilled water, and drying at 80 °C for 24 h in air, ultimately, calcined at 550 °C for 6 h. The FDU-12 samples with hexagonal prism, spiral

and brick-like morphologies were denoted as F-HP, F-SP and F-BL, respectively.

The corresponding NiMo catalysts were prepared by two-step incipient-wetness impregnation of ammonium heptamolybdate ($(NH_4)_6Mo_7O_{24}\cdot4H_2O$, Sinopharm Chemical Reagent, 99.9 wt%) and nickel nitrate ($(Ni(NO_3)_2\cdot6H_2O$, Tianjin Guangfu Fine Chemical Research Institute, 99.99 wt%). After each impregnation, the samples were dried overnight in an oven at 80 °C and calcined in air at 550 °C for 6 h. The obtained catalysts were crushed into 40–60 mesh particles. The metal composition was 12 wt% of MoO_3 and 3 wt% of NiO. The resulting catalysts were denoted as NiMo/F-HP, NiMo/F-SP and NiMo/F-BL, respectively.

2.2. Characterization of supports and catalysts

Small-angle X-ray scattering (SAXS) patterns carried out on a NanoSTAR Small-Angle X-ray scattering system (Bruker, Germany) using $Cu K\alpha$ radiation (40 kV, 35 mA).

Nitrogen sorption isotherms of the samples were measured by a Micromeritics TriStar II 2020 porosimetry analyzer at 77 K. The specific surface areas of the samples were calculated using the Brunauer-Emmett-Teller (BET) method. The total volumes of micro- and mesopores were calculated from the amounts of nitrogen adsorbed at $p/p_0 = 0.98$. The pore size distribution (PSD) was derived from the desorption branches of the isotherms using the Barrett-Joyner-Halenda (BJH) method.

Scanning electron microscopy (SEM) images were recorded on a Cambridge S-360 apparatus operating at 20 kV. Transmission electron microscopy (TEM) measurements were carried out via a JEOL2010 electron microscope at an acceleration voltage of 200 kV.

The surface acid types and amounts over the catalysts were carried out by pyridine-FTIR spectroscopy in an *in situ* FTIR cell (MAGNAIR 560) with a resolution of 1 cm^{-1} . The FTIR spectra were obtained after the system was degassed at different temperatures (200 °C and 350 °C) for 2 h.

The UV-vis diffuse reflectance spectroscopy (UV-vis DRS) experiments were recorded in the wave number of 200–800 nm using a Hitachi U-4100 UV-vis spectrophotometer with the integration sphere diffuse reflectance attachment.

The Raman spectra were obtained using a Raman spectrometer (Renishaw Micro-Raman System 2000), operating with the laser wavelength of 325 nm. The laser spot size was approximately 1–2 mm with a power of 8 mW.

The X-ray photoelectron spectra (XPS) of the sulfided catalysts were acquired on a PerkinElmer PHI-1600 ESCA spectrometer.

2.3. Catalytic activity measurement

The HDS reactions of DBT were carried out in a continuous flow, fix-bed reactor (8 mm inner diameter and 400 mm in length) loaded with 0.5 g catalyst (40–60 mesh) diluted in 3 g quartz particles. All the fresh catalysts needed to be presulfidized *in situ* for 4 h with a mixture of H_2 and 2 wt% CS_2 in cyclohexane solution at 340 °C and 4 MPa.

After sulfidation, a reactant (DBT) with the sulfur contents of 500 ppm dissolved in the solvent cyclohexane was fed into the reactor by a SP-D-3201 double-piston pump. The catalysts were evaluated under the conditions of 340 °C, 4 MPa, H_2/Oil ratio of 200 mL/mL and WHSV of 20–150 h^{-1} .

The sulfur contents of the feedstock and products were tested in a sulfur and nitrogen analyzer (RPP-2000SN, Taizhou Central Analytical Instruments Co. Ltd., P.R.China). To corroborate the product compositions, the liquid products were analyzed by using gas chromatography with a mass spectrometer (GC-MS, Thermo-Finnigan Trace DSQ) with a HP-5MS column (60 m × 0.25 mm × 0.25 μ m).

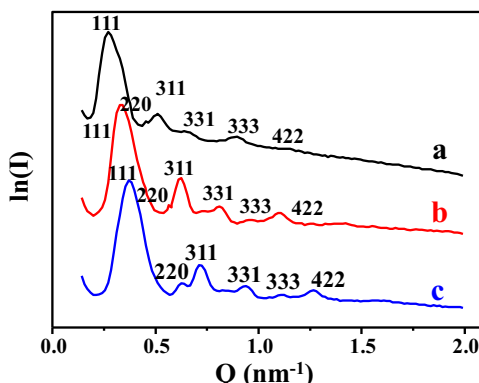


Fig. 1. SAXS patterns of the FDU-12 samples. (a) F-HP, (b) F-SP, (c) F-BL.

The catalytic performances (HDS conversion (%)) of the catalysts were calculated by Eq. (1):

$$HDS(\%) = (S_f - S_p)/S_f \times 100\% \quad (1)$$

where the S_f is the sulfur content (ppm) of the feedstock and S_p is the sulfur content of the products.

3. Results and discussion

3.1. SAXS characterization of the supports

The SAXS patterns of all samples are shown in Fig. 1. All samples exhibit five characteristic peaks, indexed as (111), (220), (311), (331) and (442) reflections respectively, as described in the literature [16], proving that they all have the structural characteristic (face-centred cubic structure Fm3m) of the mesoporous silica FDU-12.

3.2. BET characterization of the supports

The N_2 adsorption-desorption isotherms and pore distribution curves of FDU-12 with different morphologies are shown in Fig. 2(A) and (B) respectively. All the mesoporous pure silica FDU-12 show the type IV curves with a H2 hysteresis loop, which is the characteristics of ordered mesoporous structure. A sharp inflection in the adsorption-desorption isotherms is observed in the range of $P/P_0 = 0.45–0.90$ for the FDU-12 samples, which may be derives from the capillary condensation within a uniform mesostructure. The pore size distributions of F-HP, F-SP and F-BL, show a narrow distribution of mesopores. The texture parameters of FDU-12 with different morphologies are listed in Table 1. The pore diameters of the FDU-12 materials follow the order of F-SP (18.2 nm) > F-HP (17.9 nm) > F-BL (17.8 nm) which can also be obtained from pore size distribution curves shown in Fig. 2(B). However, the surface areas and pore volumes of the FDU-12 materials with different morphologies change in sequence of F-HP ($865 \text{ m}^2 \text{ g}^{-1}$, $0.79 \text{ cm}^3 \text{ g}^{-1}$) > F-SP ($861 \text{ m}^2 \text{ g}^{-1}$, $0.72 \text{ cm}^3 \text{ g}^{-1}$) > F-BL ($852 \text{ m}^2 \text{ g}^{-1}$, $0.68 \text{ cm}^3 \text{ g}^{-1}$).

Table 1

Texture parameters of FDU-12 with different morphologies.

Sample	Morphology	BET surface area [$\text{m}^2 \text{ g}^{-1}$]	Total Pore Volume [$\text{cm}^3 \text{ g}^{-1}$]	Pore diameter [nm] ^a
F-HP	hexagonal prisms	865	0.79	17.9
F-SP	spiral	861	0.72	18.2
F-BL	brick-like	852	0.68	17.8

^a Determined from the adsorption branch on the basis of BJH model.

Table 2
Textural properties of FDU-12 series catalysts with different morphologies.

Samples	Surface area/ $\text{m}^2 \text{ g}^{-1}$	External area/ $\text{m}^2 \text{ g}^{-1}$	Pore volume / $\text{cm}^3 \text{ g}^{-1}$	Pore size/nm
NiMo/F-HP	368	262	0.39	16.3
NiMo/F-SP	284	207	0.39	16.5
NiMo/F-BL	340	248	0.38	16.4

3.3. SEM characterization of the supports

The morphology of FDU-12 with different morphologies was investigated by means of field emission SEM. The SEM images of different FDU-12 samples are given in Fig. 3. It could be found that FDU-12 (in Fig. 2a) synthesized by introducing potassium chloride showed a hexagonal prisms shape. The particle size of the F-HP sample is about 6.86 μm . Spiral rodlike morphological mesoporous silica FDU-12 crystals was obtained in the presence of the inorganic salt MgSO_4 (in Fig. 2b) and the particle size of the F-SP sample is about 6.22 μm . In addition, when manganese sulfate was added to be the additive into the synthesis solution, the brick-like mesoporous FDU-12 particles with 4.12 μm in length and 2.08 μm in width (in Fig. 2c) was formed under the similar acidic conditions.

3.4. TEM characterization of the supports

Fig. 4 shows the TEM images of pure FDU-12 materials with different morphologies. The image of FDU-12 is consistent with the literature [16]. Under the TEM observations, all the FDU-12 supports synthesized under different conditions exhibit the well-ordered face-centred cubic (Fm3m) structures which accord well with the XRD results, indicating that FDU-12 is synthesized successfully.

3.5. BET characterization of the oxide catalysts

N_2 adsorption-desorption isotherms of different catalysts are shown in Fig. 5(A). It can be seen that all the catalysts show type IV isotherms with a sharp step at intermediate relative pressures. The appreciable type H2 hysteresis loops indicate the presence of textural mesopores, which means that the uniform textural porosity of FDU-12 is maintained after the catalysts preparation process. The impregnation of active metals on the supports decreases the values of surface area and pore volume due to the coverages of the support surfaces and the partial blockage of micropores [21]. Moreover, all the catalysts show similar pore size distributions in Fig. 5(B). The textural characteristics of the corresponding catalysts derived from these N_2 adsorption-desorption isotherms are summarized in Table 2. It can be seen that the NiMo/F-HP catalyst displays the highest surface area and external area.

3.6. Pyridine-FTIR analysis of the oxide catalysts

The acidities of different catalysts were investigated using the pyridine-FTIR method. Different signals can be observed in the spectra in the region of $1700–1400 \text{ cm}^{-1}$ as shown in Fig. 6. According to the literature [22], the bands at 1450 and 1610 cm^{-1} are ascribed to pyridine adsorbed onto the strong Lewis acid sites,

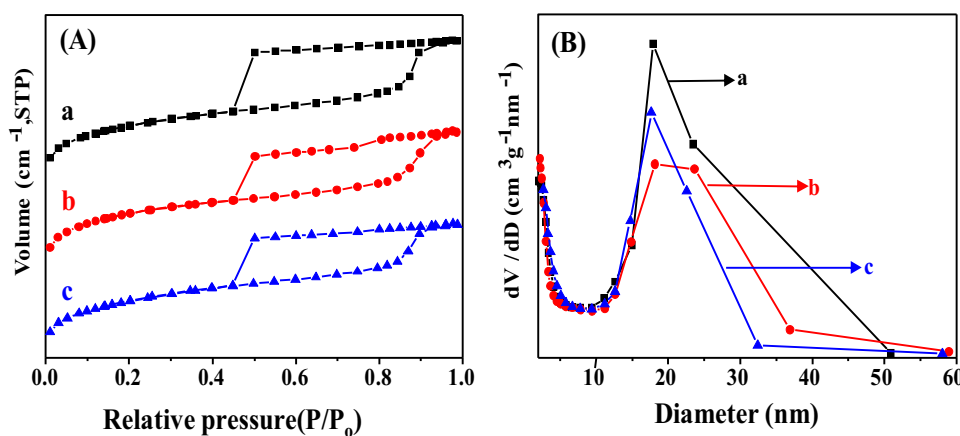


Fig. 2. (A) N₂ adsorption/desorption isotherms and (B) pore size distribution patterns of the series FDU-12 with different morphologies. (a) F-HP, (b) F-SP, (c) F-BL.

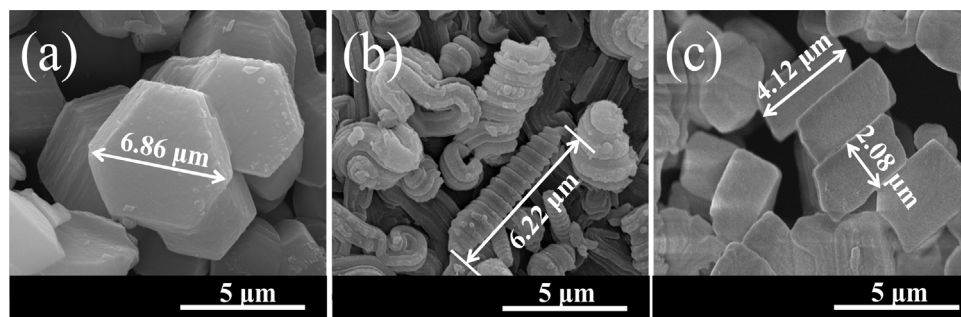


Fig. 3. The SEM images of different samples. (a) F-HP, (b) F-SP, (c) F-BL.

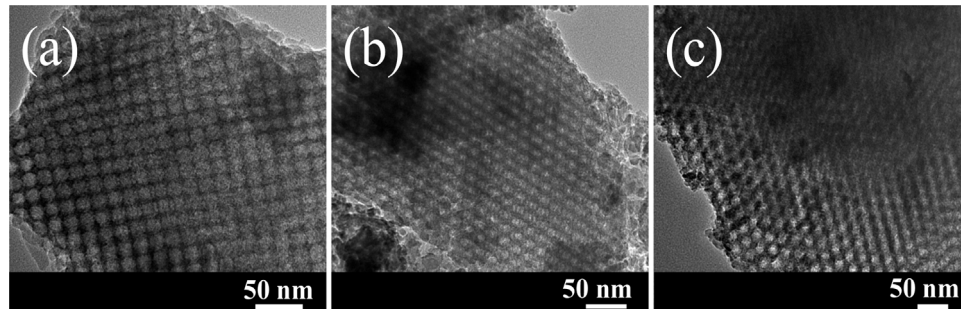


Fig. 4. The TEM images of different samples. (a) F-HP, (b) F-SP, (c) F-BL.

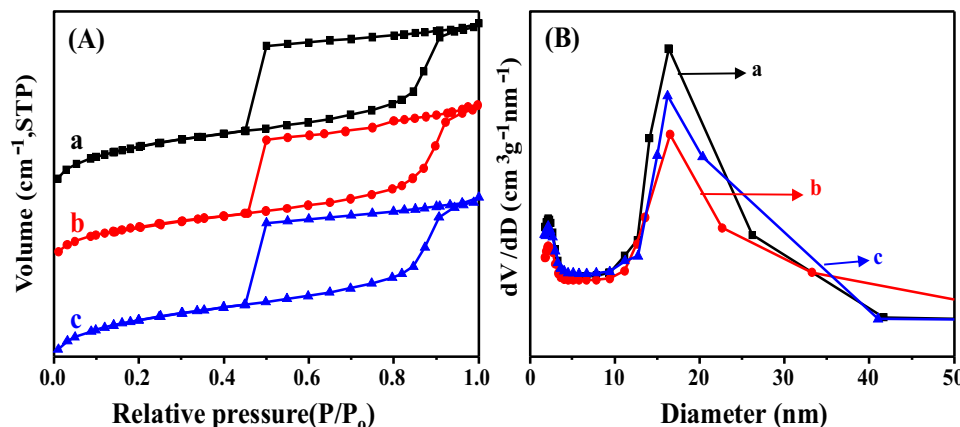


Fig. 5. (A) N₂ adsorption/desorption isotherms and (B) pore size distribution patterns of (a) NiMo/F-HP, (b) NiMo/F-SP, (c) NiMo/F-BL.

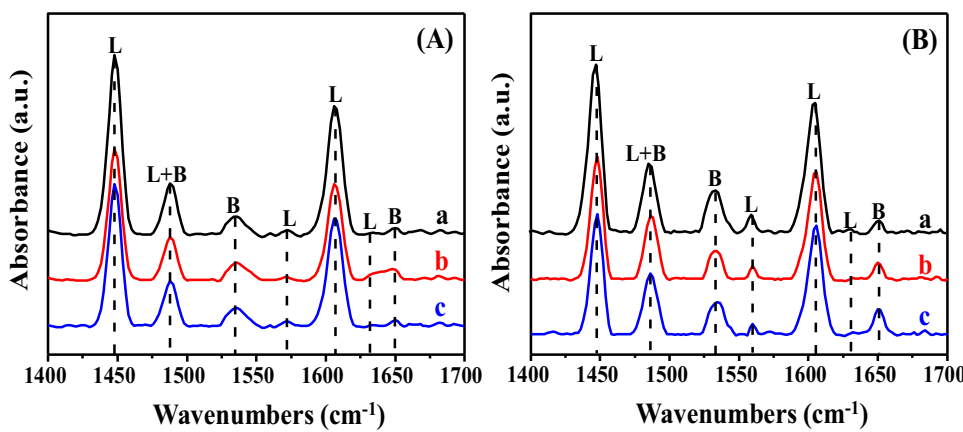


Fig. 6. FTIR spectra of pyridine adsorbed on (a) NiMo/F-HP, (b) NiMo/F-SP, (c) NiMo/F-BL after degassing at (A) 200 °C and (B) 350 °C.

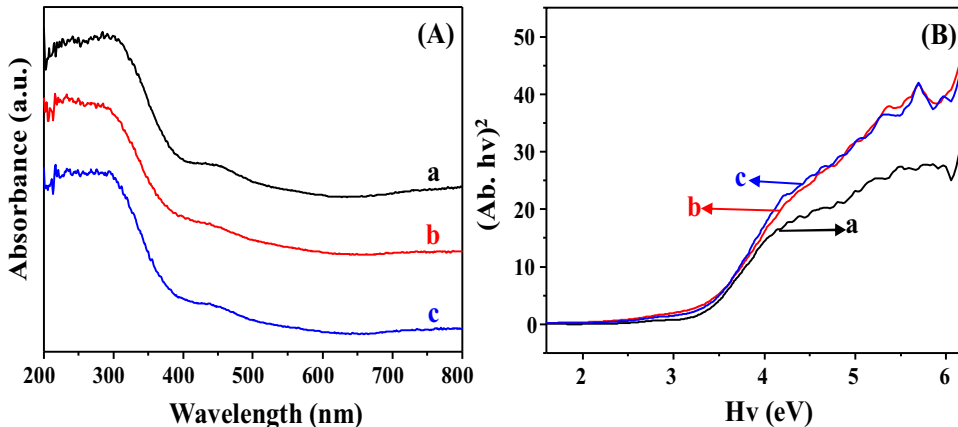


Fig. 7. (A) UV-vis DRS spectra and (B) plots of $(\alpha)^{1/2}$ versus photon energy ($h\nu$) of the oxide catalysts. (a) NiMo/F-HP, (b) NiMo/F-SP, (c) NiMo/F-BL.

while the band at 1575 cm⁻¹ is attributed to pyridine adsorbed onto the weak Lewis acid sites, and the bands at 1542 and 1640 cm⁻¹ are belonged to the pyridinium ion ring vibration owing to pyridine molecules adsorbed to Brønsted acid sites. The band at 1492 cm⁻¹ is assigned to the pyridine associated with both Brønsted and Lewis sites. The detailed data about the acid strength distribution and the acid quantity of the catalysts are listed in Table 3. These results (in Table 3) were calculated from the IR spectra collected from the catalysts with pyridine adsorption followed by degassing at 200 °C and 350 °C (the total amounts of acid sites were determined by the pyridine adsorption IR spectra after degassing at 200 °C, and the amounts of medium and strong acid sites were determined by the IR pyridine adsorption spectra after degassing at 350 °C). The total amount of acid sites and the amounts of medium and strong acid sites of the NiMo/F-HP, NiMo/F-SP and NiMo/F-BL catalysts increase in the following order: NiMo/F-HP > NiMo/F-SP > NiMo/F-BL.

3.7. UV-vis DRS analysis of the oxide catalysts

Fig. 7(A) shows UV-vis DRS spectra of three different catalysts. As previously reported [23,24], absorption in the 200–350 nm region observed in Fig. 7(A) should be assigned to ligand-to-metal charge transfer (LMCT) O²⁻ → Mo⁶⁺. It is well-known that the position of this LMCT band depends strongly on the local symmetry around the Mo⁶⁺ species and their aggregation state. The isolated molybdate species in tetrahedral coordination (Mo(Td)) show a characteristic absorption band at 220–250 nm, whereas the signal of polymolybdate species in octahedral coordination (Mo(Oh)) is observed at the 280–330 nm region and its position is affected by the aggregate sizes (the larger aggregates have the smaller energies). In addition, both types of Mo⁶⁺ species show the second strong absorption band at about 220 nm. The DRS spectra of the NiMo/FDU-12 catalysts reveal the presence of a mixture of Mo⁶⁺ oxidic species in tetrahedral and octahedral coordinations.

Band gap energy can be estimated by a plot of $(\alpha)^{1/2}$ versus photon energy ($h\nu$), the energy band gap decreased with the increase of the average particle size of molybdenum oxides in catalysts [25]. As shown in Fig. 7(B), the energy band gaps of Mo species change with the introduction of different inorganic salts. The energy band gap of Mo species of the catalysts follows the order of NiMo/F-HP > NiMo/F-SP > NiMo/F-BL, indicating that the average particle sizes of molybdenum oxides decrease and Mo species are distributed well in the NiMo/F-HP catalyst. The above results conform that the addition of different inorganic salts have a great influence on the oxidic molybdenum species and domain sizes.

Table 3

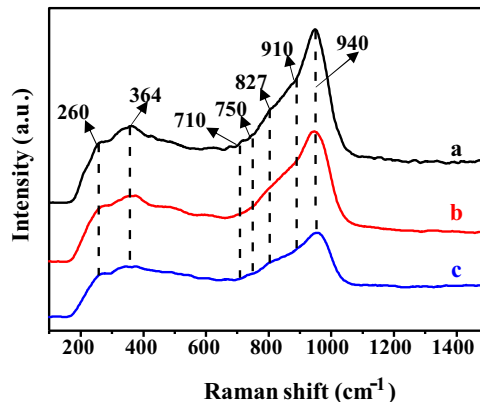
Amounts of Brønsted and Lewis acid sites determined by pyridine-FTIR of the oxide catalysts.

Catalysts	Amount of acid sites (μmol g ⁻¹)					
	200 °C			350 °C		
	L	B	L+B	L	B	L+B
NiMo/F-HP	76.4	18.4	94.8	25.6	8.7	34.3
NiMo/F-SP	68.4	18.2	86.6	22.3	7.8	30.1
NiMo/F-BL	63.6	16.3	79.9	18.2	6.5	24.7

Table 4

XPS parameters of Mo3d contributions over the sulfided NiMo catalysts.

Catalysts	Mo ⁴⁺		Mo ⁵⁺		Mo ⁶⁺		S_{Mo}^b
	ar.% ^a (228.9 eV)	ar.% (232.0 eV)	ar.% (230.5 eV)	ar.% (233.6 eV)	ar.% (232.5 eV)	ar.% (235.6 eV)	
NiMo/F-HP	40	27	1	1	18	13	67
NiMo/F-SP	36	24	1	1	23	15	60
NiMo/F-BL	34	20	1	1	26	18	54

^a ar.% means the area percentage of XPS peak.^b $S_{Mo} = Mo_{sulfidation}/(Mo^{4+} + Mo^{5+} + Mo^{6+})$.**Fig. 8.** Raman spectra of the oxide catalysts. (a) NiMo/F-HP, (b) NiMo/F-SP, (c) NiMo/F-BL.

3.8. Raman characterization of the oxide catalysts

Raman spectra of different catalysts are presented in Fig. 8. For all NiMo catalysts, five bands at 260, 364, 750, 827 and 940 cm⁻¹ are observed. The bands at 260 cm⁻¹ are assigned to the bending vibrations of Mo—O—Mo; the bands at 364 cm⁻¹ and 827 cm⁻¹ are attributed to the bending vibrations of Mo=O in tetrahedrally coordinated molybdate (MoO₄²⁻) and the 940 cm⁻¹ band is due to the stretching vibrations of Mo=O in the octahedrally coordinated polymolybdate (Mo₇O₂₄⁶⁻) [26,27]. It can be seen that the band of the NiMo/F-HP catalyst is higher than that of other two catalysts, indicating the formation of polymolybdate species which are easy to be sulfided and transformed into more active phases in the presulfiding process. Besides, there are no obvious Raman bands for MoO₃ species, which suggests that Mo species are well dispersed in the support. The high dispersion of active metals on the surface of support makes them easy to be sulfided in the presulfidation process, thus improve the catalytic activity.

3.9. XPS characterization of the sulfided catalysts

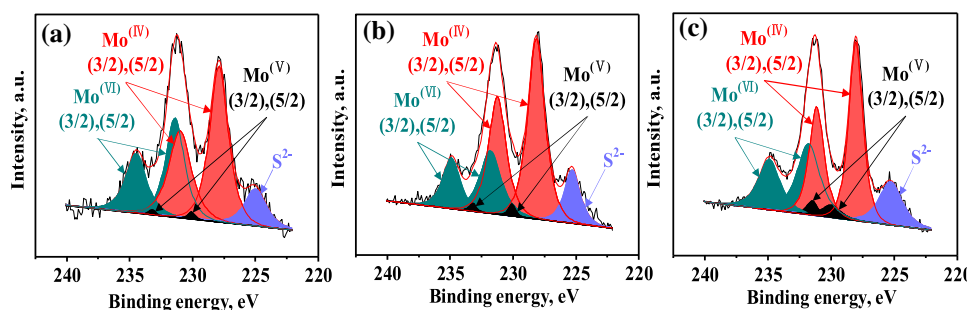
To analyze the sulfidation degrees of active metals on the surface of different supports, the fresh sulfide samples are char-

acterized by XPS and the spectra are shown in Fig. 9. The analysis results obtained by the deconvolution method [28] are summarized in Table 4. The decompositions of the Mo3d spectra have been performed simulating each contribution with two peaks corresponding to the Mo3d_{5/2} and Mo3d_{3/2} core levels, and also the binding energy difference BE (Mo3d_{5/2})-BE (Mo3d_{3/2}) is equal to 3.15 eV, while the peak area ratio of Mo3d_{5/2}/Mo3d_{3/2} is equal to 1.5 and the full width at half maximum (FWHM) of the Mo3d_{5/2} and Mo3d_{3/2} peaks are almost the same [29]. For the sulfided catalysts, the Mo3d spectra have been decomposed into the three well-known contributions, which are attributed to Mo⁴⁺, Mo⁵⁺ and Mo⁶⁺, respectively. The Mo3d envelopes for the sulfided catalysts show strong doublets at the binding energies of 228.6 ± 0.1 eV and 231.7 ± 0.1 eV, which are the characteristics of Mo⁴⁺3d_{5/2} and Mo⁴⁺3d_{3/2}, demonstrating the formation of MoS₂ species [30]. A relatively small peak at about 232.3 eV is assigned to Mo⁶⁺ species, indicating that a small proportion of Mo under oxidic form is still present after the sulfidation. The presence of Mo⁵⁺ species of oxy-sulfide phases with weak peaks at 230.5 eV can also be observed. Therefore, the envelope of Mo3d is decomposed into Mo⁴⁺ and Mo⁶⁺ components as well as one peak at about 226.0 eV which is the characteristic of S_{2s}.

The sulfidation degree of the Mo phases is assessed by using the fraction of Mo⁴⁺ species in the total Mo species. From the data in Table 3, it can be clearly seen that the values of Mo_{sulfidation}/Mo_{total}, defined as Mo(IV)/(Mo⁴⁺ + Mo⁵⁺ + Mo⁶⁺), increase in the following order: NiMo/F-BL (67%) < NiMo/F-SP (60%) < NiMo/F-HP (54%), which is in agreement with the activities of DBT HDS over these catalysts. The XPS results demonstrate that Mo species over NiMo/F-HP catalyst are easy to be sulfided compared with the other two catalysts.

3.10. Catalytic activity

Catalytic behaviors of NiMo/F-BL, NiMo/F-SP and NiMo/F-HP were evaluated in hydrodesulfurization (HDS) of the model compound, dibenzothiophene (DBT). The DBT HDS activities obtained over different LHSV values (150 h⁻¹, 120 h⁻¹, 80 h⁻¹, 50 h⁻¹ and 20 h⁻¹) are shown in Fig. 10. The HDS conversions of the supported NiMo catalysts follow the order: NiMo/F-BL < NiMo/F-SP < NiMo/F-HP. The catalyst NiMo/F-HP exhibits the highest HDS conversion,

**Fig. 9.** Mo3d XPS spectra of the sulfided catalysts. (a) NiMo/F-HP, (b) NiMo/F-SP, (c) NiMo/F-BL.

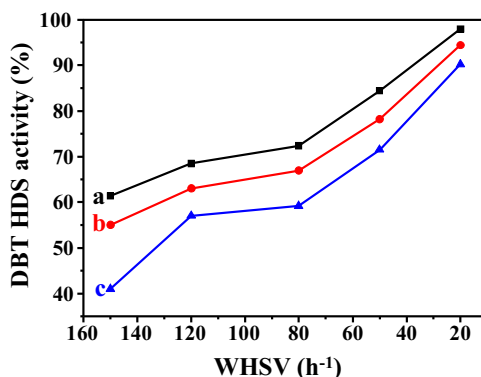


Fig. 10. HDS results of DBT at different WHSVs (340 °C, 4 MPa, 200 mL/mL). (a) NiMo/F-HP, (b) NiMo/F-SP, (c) NiMo/F-BL.

98% at the low LHSV value of 20 h⁻¹. The higher activity of the catalyst NiMo/F-HP is attributed to the synergistic effects of high external surface area, uniform structure, relative higher acidity, high dispersion degree and sulfidation degree. The external surfaces over the hexagonal prism mesoporous material distribute with mesopore cavities which make the internal surface have good connectivity. The active metals therefore can be easier to transfer into the tunnels and evenly dispersed on their surface during the preparation of catalysts. Due to the better dispersion of active metals, NiMo/F-HP catalyst had a higher degree of sulfidation which provided more active sites for the DBT HDS reactions than other catalysts. Besides, the DBT molecules can also diffuse in and out of the mesochannels from each side of the catalyst and have higher DBT conversion. In comparison to the hexagonal prism FDU-12, the mesochannel orifices of the spiral FDU-12 are unevenly distributed, indicating that the internal surface of mesochannels are not easy to be connected, while the external surface of the brick-like FDU-12 particle is significantly lower than that of hexagonal prism FDU-12. From above analyses, it can be concluded that the morphology of mesoporous FDU-12 has an important influence on catalytic performance. Besides, the proper acidity of the NiMo/F-HP catalyst can increase the interaction between the active metals and the supports, thus improving the dispersion of the active phases. Moreover, the sulfided NiMo/F-HP catalyst shows the highest sulfidation degree, which can enhance the DBT HDS activity of the catalyst.

4. Conclusion

FDU-12 silicas with three kinds of morphologies were successfully synthesized by introducing different inorganic salts. After the impregnation of Ni and Mo active metals, the mesoporous structures and the face-centred cubic (Fm3m) structures of FDU-12 with different morphologies were remained. The series of supports and the corresponding NiMo catalysts for HDS were characterized by SAXS, BET, SEM, TEM, UV-vis, Raman, pyridine-FTIR and XPS techniques. The sulfided NiMo/F-HP catalyst exhibited the highest dispersion degree and sulfidation degree which provided more active sites for the DBT HDS reactions than other catalysts. The HDS activities of DBT over different morphology catalysts followed the

order: NiMo/F-BL < NiMo/F-SP < NiMo/F-HP. The NiMo/F-HP catalyst with hexagonal prism morphology displayed the highest DBT HDS conversion (98%), which was consistent with the relatively higher acidity and the highest sulfidation degree (67%) of MoS₂ phases of the NiMo/F-HP catalyst.

Acknowledgments

This work was financially supported by the National Natural Science Foundation of China (No.21276277, 21676298 and U1463207), Opening Project of Guangxi Key Laboratory of Petrochemical Resource Processing and Process Intensification Technology (2015K003), CNPC Key Research Project and CNOOC project.

References

- [1] D.Q. Zhang, A.J. Duan, Z. Zhao, C.M. Xu, *J. Catal.* 274 (2010) 273–286.
- [2] A.J. Duan, T.S. Li, H. Niu, X. Yang, Z.G. Wang, Z. Chen, G.Y. Jiang, J. Liu, Y.C. Wei, H.F. Pan, *Catal. Today* 245 (2015) 163–171.
- [3] G.F. Wan, A.J. Duan, Y. Zhang, Z. Zhao, G.Y. Jiang, D.Q. Zhang, Z.Y. Gao, *Catal. Today* 149 (2010) 69–75.
- [4] H.D. Wu, A.J. Duan, Z. Chen, T.S. Li, R. Prins, X.F. Zhou, *J. Catal.* 317 (2014) 303–317.
- [5] Y.Y. Sun, R. Prins, *Angew. Chem. Int. Ed.* 47 (2008) 8478–8481.
- [6] Y.Y. Shu, Y.K. Lee, S.T. Oyama, *J. catal.* 236 (2005) 112–121.
- [7] T.W. Kim, F. Kleitz, B. Paul, R. Ryoo, *J. Am. Chem. Soc.* 127 (2005) 7601–7610.
- [8] K. Soni, B.S. Rana, A.K. Sinha, A. Bhattacharjee, M. Nandi, M. Kumar, D.M. Dhar, *Appl. Catal. B: Environ.* 90 (2009) 55–63.
- [9] C.T. Kresge, M.E. Leonowicz, W.J. Roth, J.C. Vartuli, J.S. Beck, *Nature* 359 (1992) 710–712.
- [10] L.X. Zhang, C.C. Yu, W.R. Zhao, Z.L. Hua, H.R. Chen, L. Li, J.L. Shi, *J. NonCryst. Solids* 353 (2007) 4055–4061.
- [11] I.I. Slowing, B.G. Trewyn, S. Giri, V.S.Y. Lin, *Adv. Funct. Mater.* 17 (2007) 1225–1236.
- [12] Y. Qin, Y. Wang, H.Q. Wang, J.S. Guo, Z.P. Qu, *Procedia Environ. Sci.* 18 (2013) 366–371.
- [13] D.W. Gao, A.J. Duan, X. Zhang, Z. Zhao, H. E, J.M. Li, H. Wang, *Appl. Catal. B: Environ.* 165 (2015) 269–284.
- [14] J. Liu, C.M. Li, Q.H. Yang, J. Yang, C. Li, *Langmuir* 23 (2007) 7255–7262.
- [15] E.M. Johansson, M.A. Ballem, J.M. Cordoba, M. Oden, *Langmuir* 27 (2011) 4994–4999.
- [16] J. Fan, C.Z. Yu, F. Gao, J. Lei, B.Z. Tian, L.M. Wang, Q. Luo, B. Tu, W.Z. Zhou, D.Y. Zhao, *Angew. Chem. Int. Ed.* 115 (2003) 3254–3258.
- [17] D.Y. Zhao, J.S. Sun, Q.Z. Li, G.D. Stucky, *Chem. Mater.* 12 (2000) 275–279.
- [18] A.S. Poyraz, C. Albayrak, Ö. Dag, 115, (2008), 548–555.
- [19] D.Y. Zhao, P.D. Yang, B.F. Chmelka, G.D. Stucky, *Chem. Mater.* 11 (1999) 1174–1178.
- [20] J.T. Tang, J. Liu, P.Y. Wang, H. Zhong, Q.H. Yang, *Microporous Mesoporous Mater.* 127 (2010) 119–125.
- [21] H. Shimada, T. Sato, Y. Yoshimura, J. Hiraishi, A. Nishijima, *J. Catal.* 110 (1988) 275–284.
- [22] R. Huirache-Acuña, T.A. Zepeda, E.M. Rivera-Muñoz, R. Navad, C.V. Loricerae, B. Pawelece, *Fuel* 149 (2015) 149–161.
- [23] T. Klímová, L. Peňa, L. Lizama, C. Salcedo, O.Y. Gutiérrez, *Ind. Eng. Chem. Res.* 48 (2009) 1126–1133.
- [24] L. Lizama, T. Klímová, *Appl. Catal. B: Environ.* 182 (2008) 139–150.
- [25] L.Q. Jing, B.F. Xin, F.L. Yuan, L.P. Xue, B.Q. Wang, H.G. Fu, *J. Phys. Chem. B* 110 (2006) 17860–17865.
- [26] S. Badoga, K.C. Mouli, K.K. Soni, A.K. Dalai, J. Adjaye, *Appl. Catal. B: Environ.* 125 (2012) 67–84.
- [27] P. Biswas, P. Narayanasarma, C.M. Kotikalapudi, A.K. Dalai, J. Adjaye, *Ind. Eng. Chem. Res.* 50 (2011) 7882–7895.
- [28] Z.K. Cao, A.J. Duan, Z. Zhao, J.M. Li, Y.C. Wei, G.Y. Jiang, J. Liu, *J. Mater. Chem. A* 2 (2014) 19738–19749.
- [29] J. Muijsers, T. Weber, R. Vanhardevelde, H.W. Zandbergen, J. Niemantsverdriet, *J. Catal.* 157 (1995) 698–705.
- [30] T. Fujikawa, M. Kato, T. Ebihara, K. Hagiwara, T. Kubota, Y. Okamoto, *J. Jpn. Petrol. Inst.* 48 (2005) 114–120.